New maps of major oxides and Mg # of the lunar surface from additional geochemical data of Chang'E-5 samples and KAGUYA multiband imager data

Liang Zhang [a], Xubing Zhang [b], Maosheng Yang [a], Xiao Xiao [a], Denggao Qiu [c], Jianguo Yan [c], Long Xiao [a], Jun Huang [a,d,*]

[a] State Key Laboratory of planetary processes and mineral resources, School of Earth Sciences, China University of Geosciences (Wuhan), Wuhan 430074, China
[b] School of Geography and Information Engineering, China University of Geosciences, Wuhan 430078, China
[c] State Key Laboratory of Information Engineering in Surveying, Mapping and Remote Sensing, Wuhan University, Wuhan 430070, China
[d] Chinese Academy of Sciences Center for Excellence in Comparative Planetology, Hefei 230026, China

ARTICLE INFO

ABSTRACT

In the past, global maps of major oxides and magnesium number (Mg #) on the lunar surface had been derived from spectral data of remote sensing images, combined with "ground truth" geochemical information from Apollo and Luna samples. These compositional maps provide insights into the chemical variations of different geologic units, revealing the regional and global geologic evolution. In this study, we produced new maps of five major oxides (i.e., Al_2O_3, CaO, FeO, MgO, and TiO_2) and Mg # using imaging spectral data from the KAGUYA multiband imager (MI) and the one-dimensional convolutional neural network (1D-CNN) algorithm. We took advantage of recently acquired geochemical information from China's Chang'E-5 (CE-5) samples. We used the coefficients of determination (R^2) and Root Mean Squared Error (RMSE) as model evaluation indicators. We compared the results with the previous machine learning algorithm models. Our study shows that the 1D-CNN algorithm model used in this study had a higher degree of fit and smaller dispersion between the "ground truth" value of geochemical information and the predicted value of spectral data. The 1D-CNN algorithm generally performs better in describing the complex nonlinear relationship between spectra and chemical components. In addition, we present regions of mare domes in Mairan Dome (43.76°N, 49.90°W) and irregular mare patches (IMPs) in Sosigenes (8.34°N, 19.07°E) to demonstrate the geologic implications of these new maps. With the highest spatial resolution (~ 59 m/pixel), these new maps of five major oxides and Mg # will serve as an important guide in future studies of lunar geology.

1. Introduction

The study of the major oxide elements (e.g., Al, Ca, Fe, Mg, and Ti) abundances and magnesium number (Mol % of Mg / (Mg + Fe), Mg #) of the lunar surface is the basic and premise for understanding the formation and evolution of the moon. Among them, iron is one of the most abundant elements in lunar silicate minerals (Wilcox et al., 2005). Titanium is used in mare basalt classification (e.g., Charette et al., 1974; Taylor et al., 1991; Giguere et al., 2000). Iron and titanium elements are important indicators for the crustal evolution of the moon (Taylor, 1987; Lucey et al., 1995, 1998; Lucey et al., 2000; Ling et al., 2010, 2011; Sun et al., 2016). In addition, the distribution of iron and titanium on the

lunar surface is also of great significance to the development and utilization of lunar resources (Heiken et al., 1991). Besides the elements of iron and titanium, the elements of aluminum, calcium, and magnesium are also major chemical compositions in lunar rock (Papike, 1988). During the crystallization of the lunar magma ocean, these minerals with different magnesium-iron ratios lead to different crystallization rates (Lucey et al., 2006). Thus, the Mg # of the lunar surface is an important indicator for understanding the evolution of the lunar magma ocean (Ohtake et al., 2012; Laneuville et al., 2017).

Various studies have shown correlations between spectra and the abundance of major oxide elements on the lunar surface (e.g., Haggerty, 1972; McCord et al., 1972; Adams and Charette, 1975; Hapke et al.,


Table 1
Contents of chemical components at sampling points of the lunar surface oxides.

| Site	Al_2O_3 (wt%)	CaO (wt%)	FeO (wt%)	MgO (wt%)	TiO_2 (wt%)
Apollo12LM	13.80	10.60	15.40	9.70	3.07
Apollo14LM	16.90	10.60	10.70	10.10	1.66
Apollo15LM	14.45	10.25	14.95	10.65	1.89
Apollo16LM	27.60	15.70	4.50	5.70	0.60
Apollo16S1	27.55	15.88	4.95	5.54	0.52
Apollo16S2	27.00	15.95	5.49	5.84	0.56
Apollo16S4	27.60	16.90	4.20	4.60	0.40
Apollo16S5	25.94	15.00	5.83	6.39	0.70
Apollo16S6	26.10	15.28	5.90	6.26	0.66
Apollo16S8	26.40	15.30	5.50	6.20	0.60
Apollo16S9	26.30	15.49	5.69	6.34	0.60
Apollo16S11	28.60	16.40	4.10	4.70	0.40
Apollo16S13	27.70	15.80	4.66	5.32	0.52
Apollo17LM	12.80	11.17	15.82	9.94	7.70
Apollo17S1	10.90	10.72	17.66	9.72	9.47
Apollo17S2	20.60	12.76	8.82	10.00	1.50
Apollo17S3	20.40	12.80	8.71	9.95	1.80
Apollo17S4	13.50	11.30	15.02	9.45	7.24
Apollo17S5	10.97	10.85	17.70	9.51	9.90
Apollo17S6	18.40	12.20	10.60	10.90	3.30
Apollo17S7	17.16	11.93	11.70	10.19	3.91
Apollo17S8	16.00	11.70	12.90	10.20	5.10
Apollo17S9	13.98	11.26	15.10	10.00	6.43
Apollo17LRV1	12.60	11.15	16.30	9.41	7.95
Apollo17LRV2	16.10	11.83	13.45	10.25	4.37
Apollo17LRV3	14.40	10.80	15.70	11.40	4.67
Apollo17LRV4	21.30	13.00	8.20	10.00	1.29
Apollo17LRV5	19.90	12.75	9.75	8.91	2.56
Apollo17LRV6	19.35	12.45	10.29	9.93	2.56
Apollo17LRV7	12.80	10.70	16.10	10.25	6.83
Apollo17LRV8	13.45	11.25	15.70	9.86	6.58
Apollo17LRV9	14.25	11.30	14.60	9.83	6.14
Apollo17LRV10	17.50	12.10	11.18	10.51	3.74
Apollo17LRV11	16.25	11.85	12.69	10.02	4.50
Apollo17LRV12	11.15	10.70	17.40	9.36	10.00
Luna16	15.30	12.50	16.60	8.80	3.40
Luna20	22.80	14.80	7.00	9.50	0.50
Luna24	15.50	13.10	16.20	8.80	1.10
CE-3	12.11	9.72	22.24	8.61	4.31
CE-5	11.60	10.90	22.20	5.80	5.70

1975; Liebermann and Ringwood, 1976; Lucey et al., 1995; Pieters et al., 2000). Major oxides maps have been produced with Lunar Reconnaissance Orbiter Wide Angle Camera (WAC) Ultraviolet/Visible (UV/VIS) data (Sato et al., 2017), China's Chang'E-1 (CE-1) Interference Imaging Spectrometer (IIM) data (Wu, 2012; Yan et al., 2012; Sun et al., 2016; Xia et al., 2019), Clementine UV/VIS data (Lucey et al., 1995; Lucey et al., 2000; Gillis et al., 2003, 2004), the Moon Mineralogy Mapper (M^3) data (Bhatt et al., 2020; Surkov et al., 2020) and KAGUYA Multiband Imager (MI) data (Otake et al., 2012; Lemelin et al., 2015, 2016; Qiu et al., 2021; Wang et al., 2021). In previous studies, FeO and TiO_2 abundances were usually obtained by establishing a linear correlation model between an angle parameter and an origin point (Lucey et al., 1995, 1998; Lucey et al., 2000; Otake et al., 2012; Wu, 2012; Yan et al., 2012). Other oxides (e.g., Al_2O_3, CaO and MgO) abundances have been derived with non-linear inversion models, including the partial least squares regression (PLSR) model (Wu, 2012; Sun et al., 2016), neural networks (NN) model (Xia et al., 2019), support vector machine (SVM) model (Bhatt et al., 2020; Wang et al., 2021) and random forest (RF) model (Qiu et al., 2021).

Geochemical data of the returned lunar samples and in situ measurements are bench marks of the oxide maps derived from orbital reflectance spectral data. The samples used in previous studies include the Apollo samples, the Luna samples and the Alpha Particle X-ray spectrometer (APXS) chemical analysis data (Fu et al., 2014) of the Chang'E-3 (CE-3) Yutu rover at northern Imbrium. In December 2020, China's Chang'E-5 (CE-5) mission returned 1.731 kg lunar samples from the northern Oceanus Procellarum (43.06°N, 51.92°W). These samples are mostly derived from local basalt (Qian et al., 2021a, 2021b; Jia et al., 2021, 2022), which erupted ~2 Ga ago (Che et al., 2021; Li et al., 2021), thus the youngest samples returned. The addition of the new sample data of CE-5 is of great value for the update of lunar surface oxide abundance maps.

The one-dimensional convolutional neural network (1D-CNN) model is a non-linear inversion model, which is demonstrated better (Chen et al., 2016; Malek et al., 2018; Qiu et al., 2021) in learning the relevant information between spectra as features from the spectral data than linear models and other machine learning models (e.g., random forest algorithm). The KAGUYA MI of preprocessing is a lunar imaging spectrometer with the highest spatial resolution (~ 59 m / pixel) (Ohtake et al., 2013). In this study, we have included the latest CE-5 sample point data on the basis of previous research work (Lucey et al., 2000; Wu,
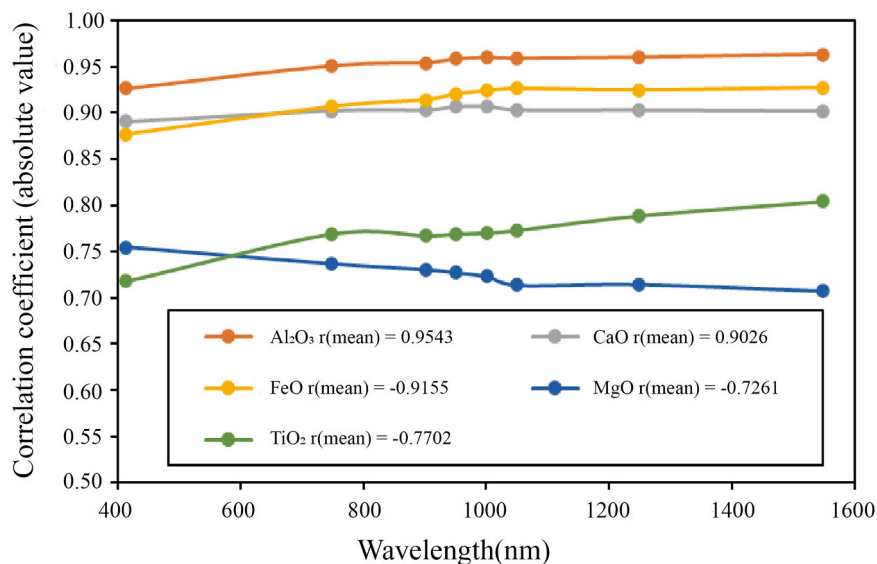

Fig. 1. Absolute values of Pearson correlation coefficient between five major oxide contents and MI reflectance values. Where, positive correlation (Al_2O_3, CaO) and negative correlation (FeO, MgO, TiO_2). The correlation coefficient was calculated from 40 lunar sampling points. The r (mean) represents the average value of the Pearson correlation coefficient in all bands.
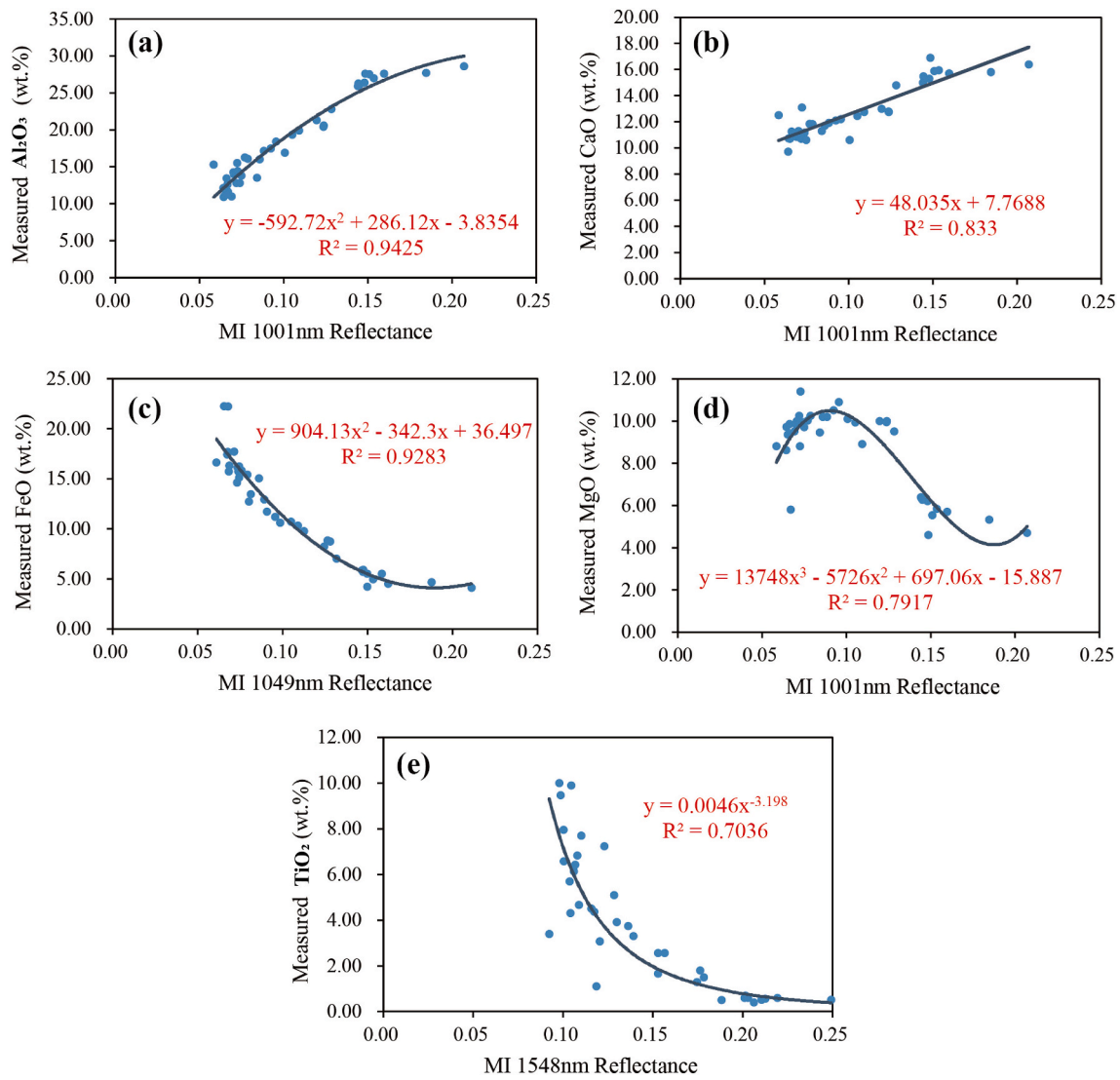
Fig. 2. Linear or nonlinear relations between (a) Al$_2$O$_3$, (b) CaO, (c) FeO, (d) MgO, and(e) TiO$_2$ contents and the reflectance values of one MI band. Only (b) is linear, and (a), (c), (d), and (e) are nonlinear.
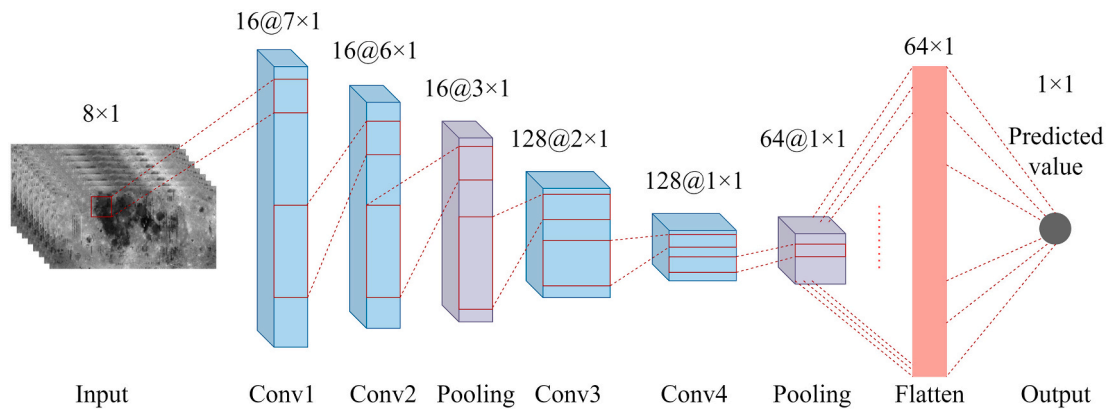
Fig. 3. Regression model of lunar major oxides based on 1D-CNN. The input layer of the network is the average spectral data of lunar sampling points with the size of 1×8. The size of convolution kernel used in convolution operation is 1×2. After the Conv1, 16 characteristic maps of 1×7 size are output; after the Conv2, 16 characteristic maps of 1×6 size are output; after down sampling, the Pooling layer outputs characteristic maps of 1×3 size; after the Conv3, 128 characteristic maps of 1×2 size are output; after the Conv4, 128 characteristic maps of 1×1 size are output; after the Pooling layer, 64 characteristic maps of 1×1 size are output; the Flatten layer pulls these characteristic maps to a vector of 1×64 size. Finally, the predicted value is output through the output layer.
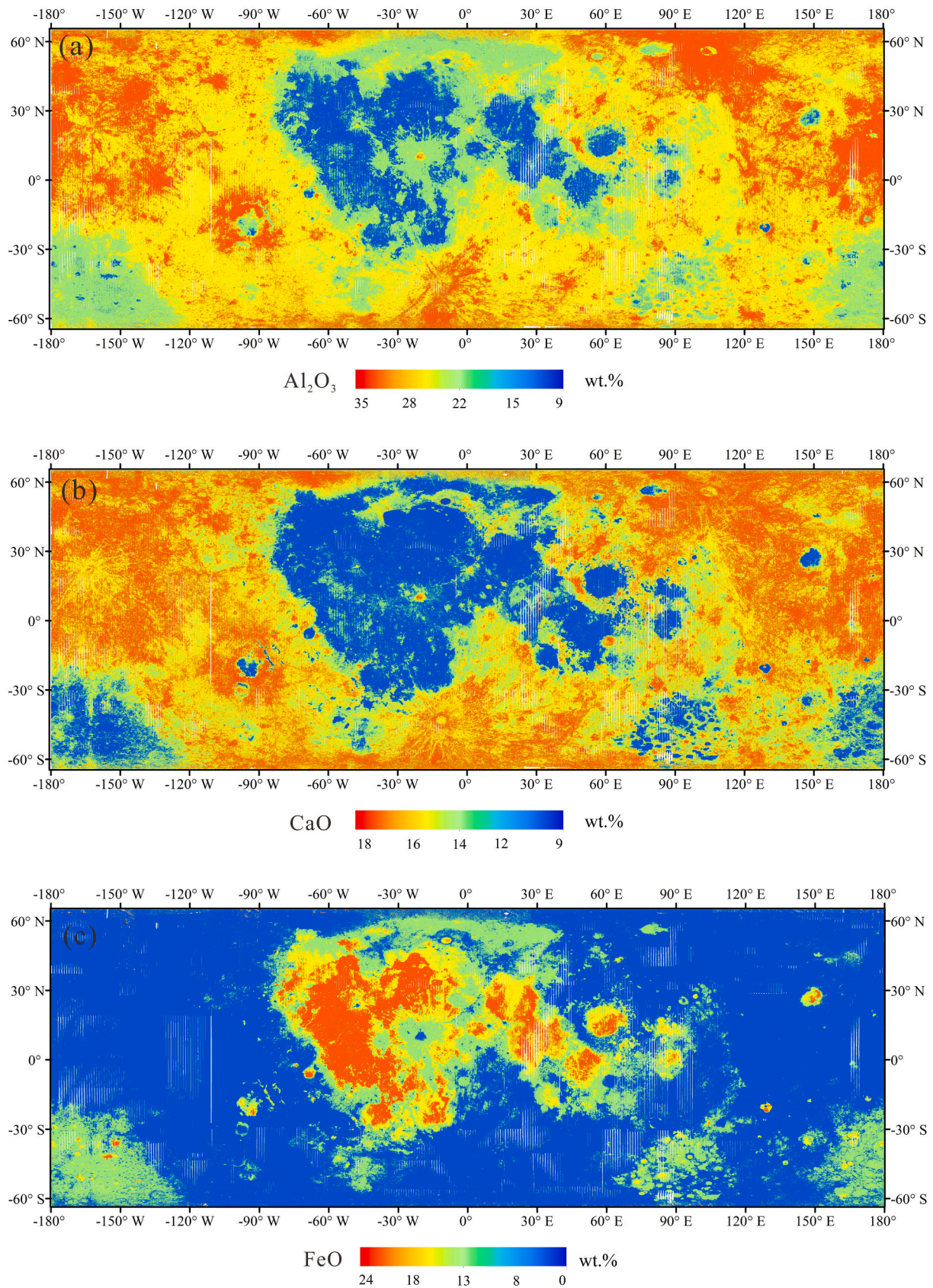
Fig. 4. Maps of (a) Al$_2$O$_3$; (b) CaO; (c) FeO; (d) MgO; (e) TiO$_2$ abundances and (f) Mg #. The Mg # map highlights the approximate boundaries of three lunar geological terranes (PKT, FHT, and SPAT) (Jolliff et al., 2000). The red lines mark the PKT unit, the blue lines encircle the SPAT unit, and the remaining region is the FHT unit. (For interpretation of the references to colour in this figure legend, the reader is referred to the web version of this article.)
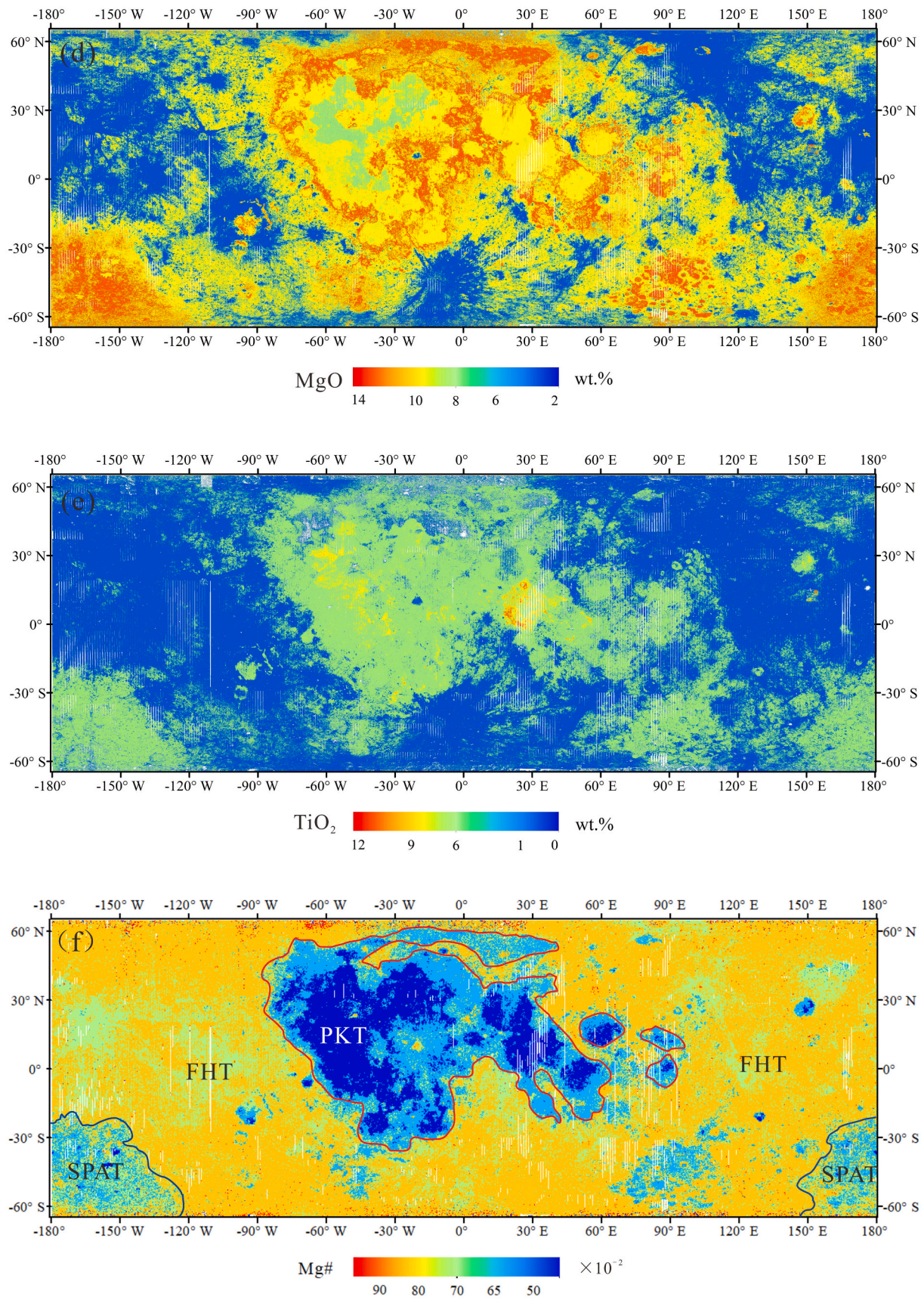
Fig. 4. (*continued*).

Table 2
Means of five oxide abundances of the moon.

	Al_2O_3 (wt%)	CaO (wt%)	FeO (wt%)	MgO (wt%)	TiO_2 (wt%)
This study					
Global	**23.44**	**14.37**	**7.42**	**7.76**	**1.34**
Mare	15.36	11.36	15.39	9.25	2.89
Highland	25.07	14.97	5.81	7.46	1.04
Global (Wu, 2012)	25.32	16.89	6.42	6.46	1.54
Global (Wang et al., 2021)	**23.56**	**14.20**	**7.40**	**7.67**	**1.15**

2012; Xia et al., 2019; Wang et al., 2021; Qiu et al., 2021) on lunar sample point data. At the same time, we have extended the deep learning algorithm to the inversion of other major oxide abundances (e.g., Al_2O_3, CaO, MgO) of the moon based on the research of Qiu et al., 2021, we use the 1D-CNN algorithm to build an optimized spectral inversion model and generate lunar surface abundance maps of five major oxides (i.e.,

Al_2O_3, CaO, MgO, FeO, and TiO_2) and Mg #. We have also selected several regions to demonstrate the usage of these new maps.

2. Data and methods

2.1. Data

The MI data includes 9 spectral bands, of which the UV/VIS band centers are 415 nm, 750 nm, 900 nm, 950 nm, and 1001 nm, and the NIR band centers are 1000 nm, 1050 nm, 1250 nm, and 1550 nm. The global mosaic covers the range from 65°N ~ 65°S on the lunar surface (Ohtake et al., 2008), with a high spatial resolution of ~59 m / pixel. We use eight bands (415 nm, 750 nm, 900 nm, 950 nm, 1001 nm, 1050 nm, 1250 nm, and 1550 nm) of the MI global mosaic to calculate the abundances of the five major oxides in this study.

For the bench mark points (Table 1), we included CE-5 samples (Tian et al., 2021; Li et al., 2022; Zong et al., 2022), Apollo samples (except for
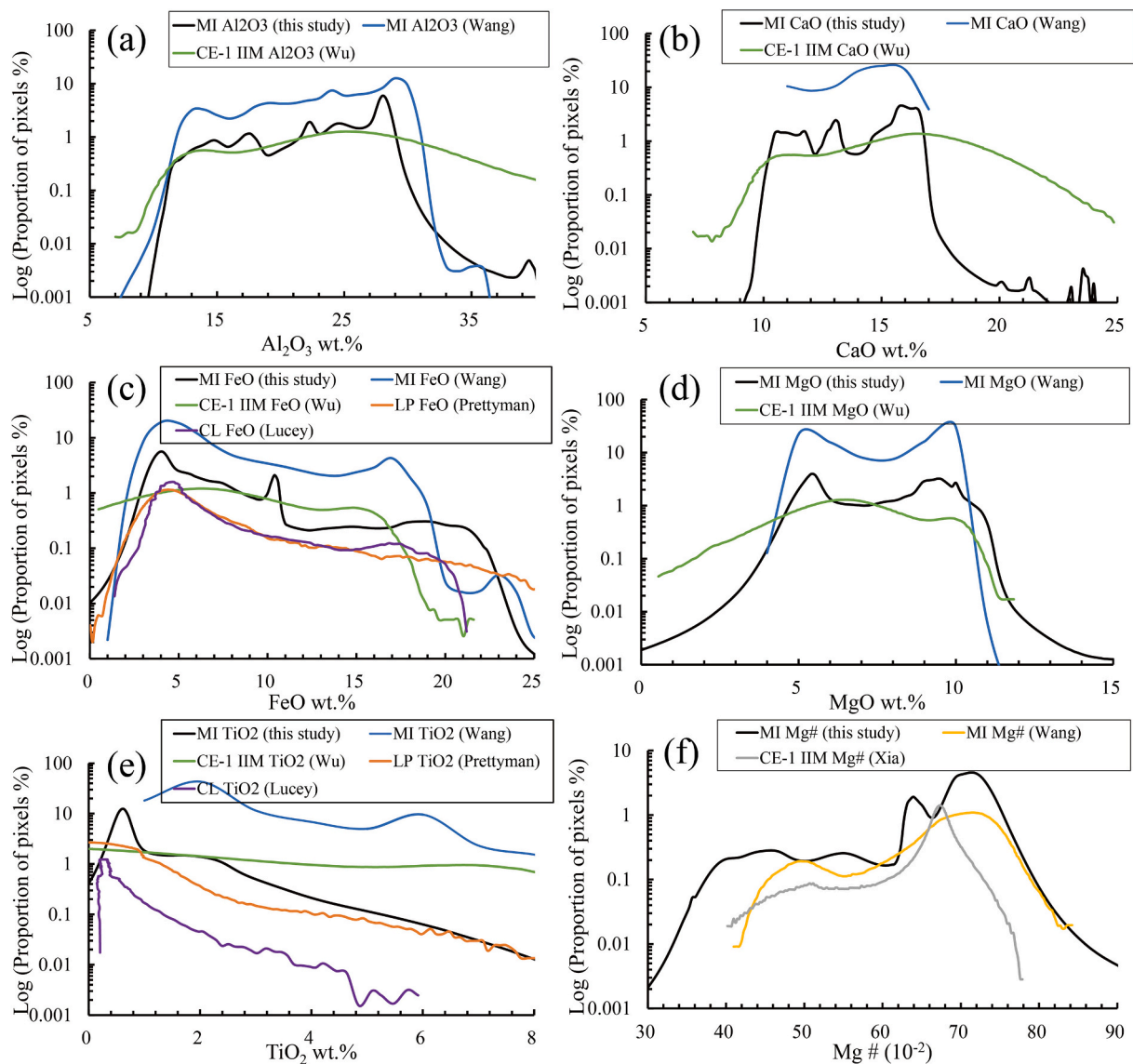
Fig. 5. Histograms of (a) Al_2O_3; (b) CaO; (c) FeO; (d) MgO; (e) TiO_2 and (f) Mg # for the lunar surface. The ordinate is the Log value of the percentage of pixels with a certain abundance in the total number of pixels. The black line is the result of this study; the blue line is the histograms of elemental abundances derived from MI data (Wang et al., 2021); the green line is the histograms of elemental abundances derived from IIM data (Wu, 2012); the orange line is the histograms of FeO and TiO_2 abundances derived from LP GNRS data (Prettyman et al., 2006); the purple line is the histograms of FeO and TiO_2 abundances derived from Clementine data (Lucey et al., 1998); the yellow line is the histograms of Mg # derived from MI data (Wang et al., 2021); the gray line is the histograms of Mg # derived from IIM data (Xia et al., 2019). (For interpretation of the references to colour in this figure legend, the reader is referred to the web version of this article.)

Table 3
The predicted values for the five oxides of the 1D-CNN model.

Site	Al_2O_3 (wt%)	CaO (wt%)	FeO (wt%)	MgO (wt%)	TiO_2 (wt%)
Apollo12LM	14.23	11.35	14.95	9.99	2.92
Apollo14LM	16.77	10.68	10.75	10.11	1.61
Apollo15LM	15.19	10.47	14.81	10.57	1.73
Apollo16LM	27.40	15.75	4.84	5.70	0.49
Apollo16S1	27.34	15.96	4.94	5.46	0.41
Apollo16S2	27.22	15.84	5.10	5.76	0.49
Apollo16S4	26.92	15.96	5.08	5.41	0.43
Apollo16S5	26.09	15.63	5.65	6.34	0.55
Apollo16S6	26.04	15.58	5.76	6.32	0.57
Apollo16S8	26.47	15.67	5.48	6.02	0.55
Apollo16S9	26.00	15.57	5.77	6.38	0.57
Apollo16S11	28.54	16.38	4.14	4.81	0.27
Apollo16S13	27.70	15.88	4.69	5.34	0.44
Apollo17LM	13.20	11.45	16.19	9.96	7.89
Apollo17S1	10.66	11.05	17.94	9.48	9.84
Apollo17S2	20.64	12.93	8.55	9.99	1.36
Apollo17S3	20.43	12.80	8.69	10.01	1.71
Apollo17S4	14.43	11.54	14.73	9.55	7.03
Apollo17S5	11.91	10.98	16.82	9.67	8.86
Apollo17S6	18.30	12.25	10.67	10.89	3.23
Apollo17S7	16.61	11.93	11.80	10.23	4.01
Apollo17S8	16.01	11.77	12.87	10.18	4.97
Apollo17S9	13.44	11.07	15.13	10.28	6.64
Apollo17LRV1	12.74	11.06	16.30	9.72	7.64
Apollo17LRV2	15.27	11.55	13.58	10.17	4.66
Apollo17LRV3	14.24	11.04	15.54	11.04	4.83
Apollo17LRV4	20.90	12.97	8.55	10.00	1.33
Apollo17LRV5	19.85	12.79	9.77	8.93	2.50
Apollo17LRV6	19.32	12.50	10.33	9.94	2.50
Apollo17LRV7	13.45	10.99	16.02	10.26	6.23
Apollo17LRV8	13.21	11.09	16.05	9.73	6.86
Apollo17LRV9	13.60	11.03	15.00	10.15	6.11
Apollo17LRV10	17.57	12.18	11.15	10.58	3.57
Apollo17LRV11	15.49	11.50	13.46	10.29	4.00
Apollo17LRV12	11.53	11.02	17.33	9.40	9.57
Luna16	15.07	11.87	17.44	8.92	3.41
Luna20	22.53	14.71	7.27	9.53	0.48
Luna24	14.42	12.03	16.87	8.65	1.15
Chang'E 3	12.33	10.82	21.70	8.35	4.08
Chang'E 5	11.63	10.95	21.98	6.43	5.54

Apollo 11, whose sampling site is not covered by the MI global mosaic), Luna samples, and in situ measurements of CE-3 rover (Zhang et al., 2015; Ling et al., 2015). In order to reduce the noise impact of MI data, we selected the average reflectance value of bench mark points in the 2 × 2 or 3 × 2 pixels to represent the "ground truth" geochemical information (Dataset S1).

2.2. Methods

2.2.1. Correlation coefficients between oxides and MI spectra

High Pearson correlation coefficients exist between MI spectra and oxide content (Fig. 1), therefore, MI spectral reflectance values can be used to retrieve the abundances of five oxides. In Fig. 2, for each oxide, an MI wavelength (e.g., 1001 nm, 1049 nm, 1548 nm) is used as an example to show the correlation between MI spectral reflectance values and oxide content, in which univariate linear or polynomial regression models for some major oxides (e.g., CaO and FeO) can obtain good fitting results. However, the oxide of TiO_2 is difficult to calculate with traditional univariate regression models due to their complex relationship with the spectra in Fig. 2e. Therefore, we use the 1D-CNN algorithm to get the abundances of all five major oxides on the lunar surface.

2.2.2. The convolutional neural network model

Convolution neural network (CNN) as one of the representative deep learning algorithms, it was initially applied to image recognition and classification in the field of computer vision (Lecun et al., 1998). Later, some researchers (Malek et al., 2018; Chen et al., 2019; Qiu et al., 2021;

Yuan et al., 2022) introduced CNN into the field of spectral analysis, the problem of regression analysis was solved by establishing a complex nonlinear correlation model between spectral data and target indicators. CNN belongs to the feedforward neural network, which is generally composed of convolution layers, pooling layers, and fully connected layers.

In the convolution layer, the convolution kernel slides on the data signal to complete feature extraction, and then the nonlinear activation function is used to output the feature vector. The CNN activation function usually selects Rectified Linear Unit (ReLU) with faster calculation speed and convergence speed (Glorot et al., 2011). The ReLU is calculated by:

$$f(x) = max(0, x) \tag{1}$$

The convolution operation process is:

$$y = f\left(\sum_i w_i x_i + b\right) \tag{2}$$

where y is the output result after weighted average of the convolution layer; w_i is the weight of the convolution kernel; b is the offset parameter.

After the convolution layer, there is a pooling layer, which is usually used for data dimension reduction, downsampling, and feature map compression. The fully connected layer is usually set before the network output layer, which is used to convert the two-dimensional feature map of convolution output into a one-dimensional feature vector to realize the end-to-end learning process.

Based on the CNN network principle, we used the 1D-CNN to build a nonlinear regression model to describe the relationship between measured oxide content and reflectivity of each sampling area (Dataset S1). 1D-CNN can avoid the extraction of information from other non-important elements, which can improve the learning efficiency of the network. Meanwhile, 1D-CNN adopts a weight-sharing mechanism, which can greatly reduce the number of parameters of the whole network, which is very important to improve the regression efficiency of the network. As shown in Fig. 3, the 1D-CNN includes 4-layer convolution layer, 2-layer pooling layer and 1-layer full connected layer in this study. The input data of the network corresponds to the spectral reflectance values of 8 bands of MI multispectral data. Feature vectors are extracted by the convolution layer. Then, in order to avoid the overfitting problem, the size of the feature vector is compressed by the pooling layer. Then, the feature map is converted into a one-dimensional feature vector through the fully connected layer. Finally, the extracted features are converted into the corresponding sample chemical composition data (i.e., the predicted value of oxide content) through the linear activation function.

2.2.3. Model parameters and evaluation index

In order to ensure the training effect of the 1D-CNN network model designed, it is necessary to set the relevant parameters of the network model. During the training phase, the Adam algorithm (Kingma and Ba, 2014) was selected for adaptive adjustment of the model weight. At the same time, the model batch size was set to 10. In addition, to evaluate the effectiveness of the training model, the sample data was divided into training and validation sets according to the ratio of 9:1 (i.e., Input 10 sample data, 9 for training, and 1 for validation). The ReLU was selected as the model activation function. The learning rate and the training iterations were set as 0.001 and 500 epochs. The model was implemented in Python using Keras framework (Ketkar, 2017).

For small sample data sets, both model training and model error estimation often lead to inaccurate error estimation results. In order to obtain a more reasonable and accurate evaluation of the model, cross-validation is used to evaluate the model. The cross-validation method selected in this study is k-fold cross-validation (KCV) (Anthony and Holden, 1998). The KCV consists in dividing the training set into k parts,
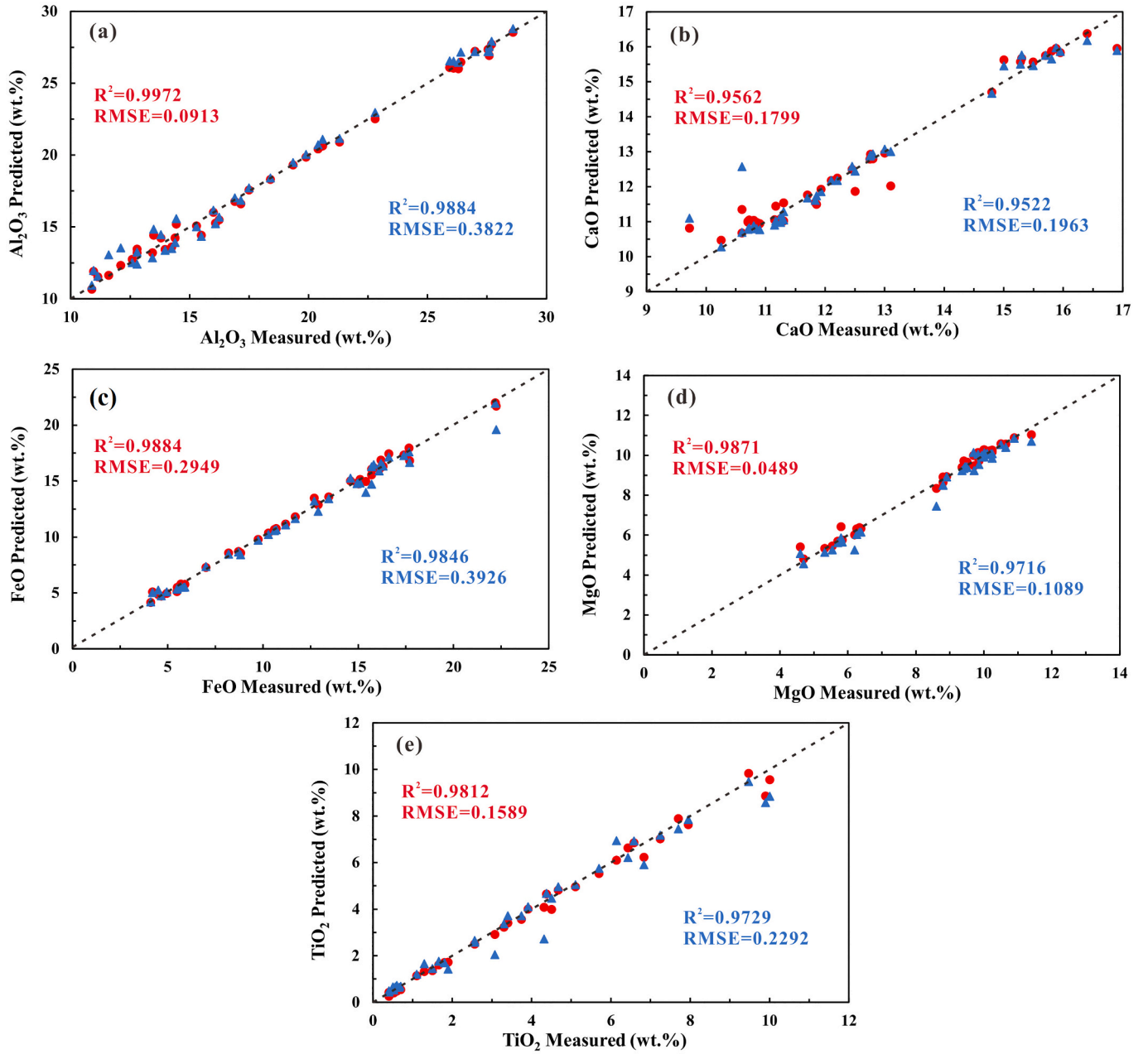
Fig. 6. Scatter plots of prediction and verification accuracies of (a) Al_2O_3, (b) CaO, (c) FeO, (d) MgO and (e) TiO_2. The red dots indicate the prediction precisions by the 1D-CNN, and the blue triangles portray the validation accuracies by k-fold cross validation. (For interpretation of the references to colour in this figure legend, the reader is referred to the web version of this article.)

each consisting of l / k samples: k – 1 parts are used, in turn, as a training set and the remaining one is used as a validation set (Anguita et al., 2009). In this study, 40 samples (spectral parameters and measured oxide abundances from 40 sample-return sites) are divided into 10 sample subsets of equal size (k = 10), and the 10 subsets are traversed in turn. Each time, the current subset is used as the verification set, and all the other samples are used as the training set for model training and evaluation.

The regression model evaluation indicators selected in this study are the coefficient of determination (R^2) and Root Mean Squared Error (RMSE).

R^2 is usually used to measure the degree of prediction results of statistical models. The value range is 0– 1. (i.e., the better the prediction ability of the model, the closer R^2 is to 1). The formula for calculating R^2 is as follows:

$$R^2(y, \widehat{y}) = 1 - \frac{\sum_{i=0}^{n}(y_i - \widehat{y}_i)^2}{\sum_{i=0}^{n}(y_i - \overline{y})^2} \tag{3}$$

where y represents predicted sampling point data; $\widehat{y}_i$ represents real sampling point data; $\overline{y}$ represents the average value of real sampling point data.

RMSE is used to measure the deviation between the predicted value and the true value. The formula for calculating RMSE is as follows:

$$RMSE(y, \widehat{y}) = \sqrt{\frac{1}{n}\sum_{i=1}^{n}\|y_i - \widehat{y}_i\|_2^2} \tag{4}$$

Table 4
Comparison of five major the performance of different models derived from this study with Wang et al. (2021) and Xia et al. (2019) models.

	Al$_2$O$_3$ (wt%)	CaO (wt%)	FeO (wt%)	MgO (wt%)	TiO$_2$ (wt%)
This study					
R^2	**0.997**	0.956	0.988	0.987	0.981
RMSE	**0.091**	**0.180**	0.295	**0.049**	**0.159**
Wang et al. (2021)					
R^2	0.973	0.847	0.940	0.952	0.877
RMSE	0.933	0.723	0.655	0.392	0.647
Xia et al. (2019)					
R^2	0.995	**0.961**	**0.998**	**0.992**	**0.989**
RMSE	0.416	0.397	**0.213**	0.164	0.322

3. Results

3.1. Maps of the major elements and Mg

The global maps of five major oxides and Mg # are shown in Fig. 4. From the perspective of the global, these oxides exhibit the characteristics of dichotomous distributions between the maria and the highlands. For example, the major oxides of Al$_2$O$_3$, CaO and TiO$_2$, FeO, MgO present an obvious negative correlation distribution in the maria. The least Al$_2$O$_3$ and CaO are present in the central regions of Mare Imbrium, Oceanus Procellarum, Serenitatis, and Tranquillitatis, but more in the boundary regions between the maria and highlands, while it is the opposite for TiO$_2$, FeO and MgO. In addition, ray materials of some craters (e.g., Tycho crater) are prominent in the maps of the major oxides, especially Al$_2$O$_3$ and CaO (Fig. 4a and Fig. 4b). We identify that the bottom and eastern parts of Tycho crater are elevated in Al$_2$O$_3$ and CaO. The global average Mg # is 0.675 is very close to the MI Mg # reported (0.67) by Wang et al. (2021), but higher than the CE-1 IIM-derived Mg # (0.644, Wu, 2012; 0.646, Xia et al., 2019), the Clementine optimized Mg # (0.57, Crites and Lucey, 2015), the LP GRS Mg # (0.606, Prettyman et al., 2006) and the Diviner Mg # (0.652, Ma et al., 2022). The average Mg # in maria is 0.527, while that of the highlands is 0.705. With the characteristics of the Mg #, we are able to distinguish the boundaries of three crustal terranes of the lunar surface (Fig. 4f, red polyline, and blue polyline) including the Feldspathic Highland Terrane (FHT), the South Pole-Aitken Terrane (SPAT), and the Procellarum KREEP Terrane (PKT)

proposed by Jolliff et al. (2000).

3.2. Comparison with previous work

The systematic differences in the average abundances of major oxides (e.g., Al$_2$O$_3$, CaO, FeO, MgO, and TiO$_2$) in the maria, highlands, and global (Table 2) are presented. The global abundance of Al$_2$O$_3$ and CaO in this study are 23.44 wt% and 14.37 wt%, Close to 23.56 wt% and 14.20 wt% proposed by Wang et al. (2021), less than 25.32 wt% and 16.89 wt% proposed by Wu (2012). The global abundance of FeO and MgO in this study are 7.42 wt% and 7.46 wt%, close to 7.40 wt% and 7.67 wt% of Wang et al. (2021), higher than 6.42 wt% and 6.46 wt% of Wu (2012). The global abundance of TiO$_2$ in this study is 1.34 wt%, higher than 1.15 wt% of Wang et al. (2021), less than 1.54 wt% of Wu (2012). In addition, the Table 2 focuses on the comparison of the global average abundance of major oxides(e.g., Al$_2$O$_3$, CaO, FeO, MgO, and TiO$_2$). The bold content is the similarity between the results of this paper and the results of previous studies. The absolute values of the differences between Al$_2$O$_3$, CaO, FeO, MgO and TiO$_2$ are 0.12, 0.17, 0.02, 0.09 and 0.19. The global results of major oxide abundance are not significantly different from those of Wang et al. (2021).

The histograms of the five oxide abundances and Mg # are shown in Fig. 5, respectively. Except for TiO$_2$ with unimodal continuum distribution characteristics, all other oxides present bimodal distributions, excluding spike interference, corresponding to Maria and Highland respectively, generally consistent with previous studies on the distribution difference of major elements in the maria and highlands (Lucey et al., 1998; Gillis et al., 2004; Prettyman et al., 2006; Wu, 2012; Lu et al., 2021). For example, the lower modal Fe abundance of ~4.12 FeO wt% and the higher modal Fe abundance of ~18.23 FeO wt%, which correspond to the highland areas and mare areas, respectively, are a little lower than the abundance of ~5.57 wt% given by Wu (2012), close to the abundance of ~4.1 wt% given by Wang et al. (2021), or ~ 4.7 wt % and ~ 4.82 wt% given by Prettyman et al. (2006) and Lucey et al. (1998).

4. Discussion

4.1. Model accuracy evaluation

The 1D-CNN model establishes a nonlinear regression model between the MI 8 band spectra and 40 sampling points by learning the data characteristics between the MI 8 band spectra and the true values of 40
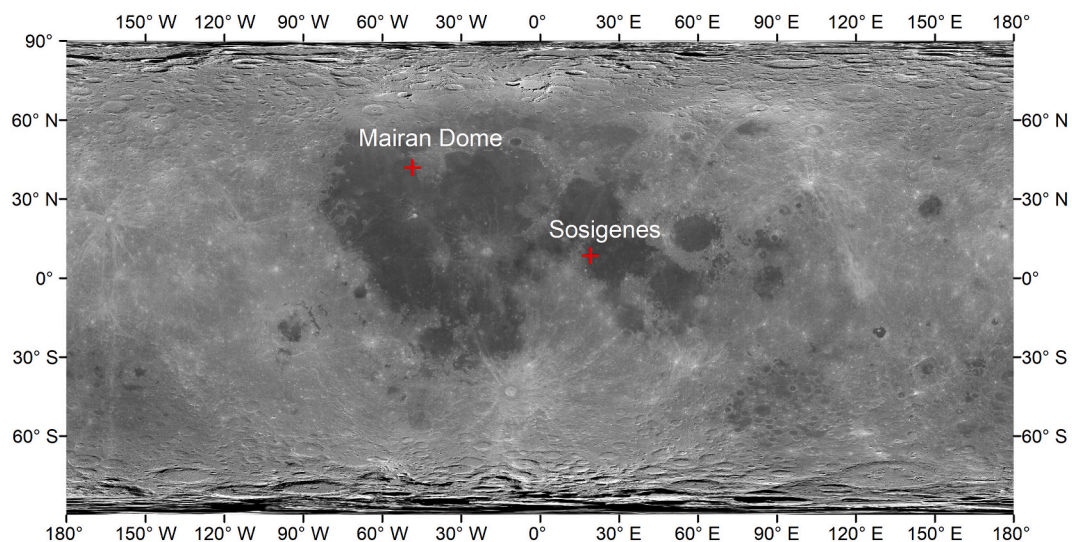
Fig. 7. Location map of the region of interest includes Mairan Dome (43.76°N, 49.90°W) and Sosigenes (8.34°N, 19.07°E). The background is CE-1 Digital Orthophoto Map (DOM) of 120 m/pixel.
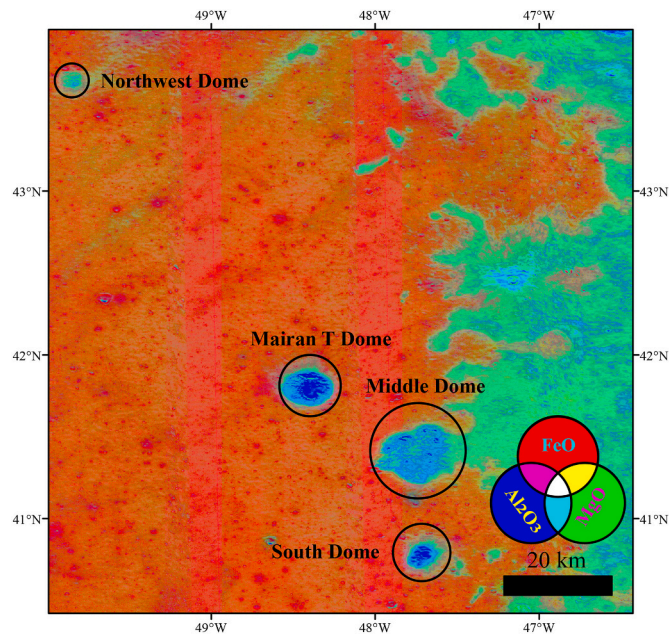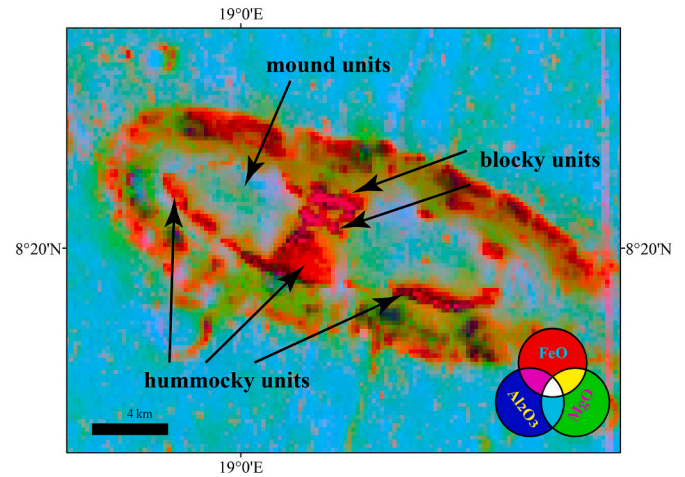
Fig. 8. Colour composite image of Mairan Domes. The red channel is FeO abundance (stretched from 0.50 to 31.10). The Green channel is MgO abundance (stretched from 1.48 to 13.81). The blue channel is Al$_2$O$_3$ abundance (stretched from 9.17 to 32.50). Black lines correspond to the boundaries of the domes as determined from the oxides content and the digital elevation model (DEM) based on Lunar Orbiter Laser Altimeter (LOLA) on board the Lunar Reconnaissance Orbiter mission (LRO). (For interpretation of the references to colour in this figure legend, the reader is referred to the web version of this article.)

Table 5
Five major oxide content of the Mairan Domes.

	MgO (wt%)	Al$_2$O$_3$ (wt%)	CaO (wt%)	TiO$_2$ (wt%)	FeO (wt%)
Northeast	9.64	17.78	12.05	3.54	12.79
Mairan T	8.40	21.95	13.61	1.56	8.95
Middle	9.26	19.15	12.19	2.72	11.86
South	8.83	21.52	13.39	1.76	9.06
mare	8.01	12.27	10.85	6.33	20.68
highlands	10.54	17.69	11.59	3.27	10.51

sampling points, so that the major oxide abundance information of the sampling points can be retrieved based on the MI spectral data, and the data inversion results from 40 sampling points can be obtained. In Table S1, we discussed the impact of convolution kernel_size on 1D-CNN model. Through comparative analysis, we determined that the network model is optimal when the final convolution kernel_size is 2. Then, based on the optimal network model, the inversion of major oxides on the lunar surface is carried out. The effect of 1D-CNN model is evaluated by calculating R^2 and RMSE between the measured and predicted values of 40 sampling points (Table 3). The prediction accuracies of the 1D-CNN and the verification accuracies of KCV for five oxides are shown in Fig. 6. The R^2 values for the oxide abundances of the prediction and validation are all greater than 0.95 and greater than 0.98 for Al$_2$O$_3$ and FeO, especially. In addition, in order to further verify the accuracy of 1D-CNN model, we have evaluated the accuracy of the training dataset (90%) and verification dataset (10%) in Table S2.

To further illustrate the advantages of 1D-CNN model, a comparison of five major oxide abundances derived from this study with Wang et al. (2021) and Xia et al. (2019) is shown in Table 4. The optimal value of the model evaluation result is bold. Compared with the inversion results of Wang et al. (2021), the 1D-CNN model in this study has higher R^2, and

the regression model fitting effect is better; Compared with the results of Xia et al. (2019), their R^2 is equivalent, but the RMSE value of 1D-CNN model is lower, and the dispersion of the inversion data of regression model is lower. On the whole, compared with the former two models, the accuracy of this research model is relatively better.

On a global scale, we also compare the new maps of major oxides in this study and the maps of Wang et al. (2021) within the range 65°N ~ 65°. These maps are generally consistent (Fig. S1).

Fig. 9. Colour composite image of Sosigenes. The red channel is FeO abundance (stretched from 15.50 to 25.58). The Green channel is MgO abundance (4.31 to 9.43). The blue channel is Al$_2$O$_3$ abundance (7.52 to 17.12). The black arrows indicate the identified Mound units、Hummocky units and Blocky units. (For interpretation of the references to colour in this figure legend, the reader is referred to the web version of this article.)

Table 6
Five major oxide content of Sosigenes.

	MgO (wt%)	Al$_2$O$_3$ (wt%)	CaO (wt%)	TiO$_2$ (wt%)	FeO (wt%)
Mound units	8.41	13.87	13.05	6.83	18.36
Hummocky units	6.65	8.41	11.49	11.67	20.41
Blocky units	6.35	10.41	11.65	10.07	20.35
mare	8.66	15.53	13.12	4.83	17.83

4.2. Regional analysis

We selected two compositionally interesting regions shown in this study (Fig. 7), including Mairan Domes (43.76°N, 49.90°W) and Sosigenes (8.34°N, 19.07°E). We added the major oxide abundance distribution content (Table S5, Fig. S3 and Fig. S4) in the Mairan Domes and Sosigenes regions, and compared the results of this study with those of Wang et al. (2021). By analyzing the inversion results of five major oxides to demonstrate the geologic implications of these new maps.

4.2.1. Mairan domes
Lunar mare domes are rounded to somewhat irregular convex landforms. They are characterized by a lower slope (generally less than 5°) and can reach a diameter of 30 km (Head and Gifford, 1980). Lunar mare domes can be divided into two different types. One type is mainly located in the center of the mare likely Marius Hills. The composition of these domes is similar to the background. The others are distributed near the highlands of the mare. Their composition is quite different from the surrounding mare basalt. Head and Gifford (1980) consider that the two types of domes are related to the interaction of lava deposits with pre-existing topography by draping or kipuka formation and primary lava vent areas.

We analyzed Mairan Domes in this study (Fig. 8). The Mairan Domes are a group of four domes at the northeast of Oceanus Procellarum near the highlands (Glotch et al., 2011). The four domes are Northeast Dome, Mairan T Dome, Middle Dome, and South Dome from north to south, respectively. Five elements content of Mairan Domes are shown in Table 5. The four domes have a significant difference in composition with the surrounding mare. The domes have FeO abundances ranging from 9 to 13 wt% FeO. This means that the domes were formed at a different time than the surrounding mare. The Northeast Dome has very close components to the highlands of the east. However, the other three domes also have some differences with the composition of the highlands, especially the Middle Dome. Although the Middle dome is partly bordered by the highlands, there are significant differences in the content of Al_2O_3. The Al_2O_3 contents of the three domes (Mairan T, Middle, and South) are higher than the highlands and Northeast Dome. This suggested that the origin of Northeast Dome may be different from the other three domes. Based on our model, the Al_2O_3 content of the units from high to low are the Mairan T Dome, South Dome, Middle Dome, Northeast Dome, highlands, and surrounding mare in the Mairan Domes region.

4.2.2. Sosigenes

IMPs are characterized by their young and small irregularly shaped depression composed of mounds and hummocky and blocky terrains (Qiao et al., 2020). Most of the IMPs are distributed in the mare unit from 3.9 to 3.1 Ga ago, suggesting that their origin may be related to the peak period of global lunar volcanism (Braden et al., 2014).

We analyzed Sosigenes in this study (Fig. 9). Sosigenes (8.34°N, 19.07°E) was discovered by Stooke (2012) in the image of the Lunar Reconnaissance Orbiter Narrow Angle Camera (LROC NAC). Qiao et al. (2018) produced a Geologic sketch map of Sosigenes. The Sosigenes IMP floor can be divided into three units according to morphology (i.e., Mound Units, Hummocky Units, and Blocky Units) (Qiao et al., 2018).

Five elements content of Sosigenes are shown in Table 6. Our oxide diagrams clearly distinguish the three units, indicating a huge difference in the oxide composition of the three units (Fig. 9). Mound Units are characterized by high MgO, CaO, Al_2O_3 and low TiO_2 compared with the other two units likely surrounding mare. Hummocky Units have a similar oxide composition to Blocky Units, with the main difference being Al_2O_3. Hummocky Units have lower Al_2O_3 than Blocky Units.

5. Conclusions

This study complements the data of the CE-5 sampling point based on the previous sampling point data and reports the new maps of five major oxides and Mg # on the moon of high spatial resolution (~ 59 m / pixel). The 1D-CNN model, one of the deep learning algorithms, was selected as the method. The prediction results of the 1D-CNN model were compared with Xia et al. (2019) and Wang et al. (2021) models. The 1D-CNN model had higher R^2 ($R^2 \rightarrow 1$) and lower RMSE, which implied that it had a satisfactory generalization ability and high fitting degrees. It could make a good quantitative prediction of the major oxide content on the lunar surface by establishing a linear and complex nonlinear relationship between spectra and the abundance of elements. By analyzing the major oxide content of lunar mare domes and IMPs in the study area, we found that there is a certain difference between the major oxide content of formation and lithology in the study area. Thus, these new maps of major oxides will serve as an important guide in the future study of lunar geology.

Open research

All data are provided in this article and its supplementary materials. The Mg # and the abundances of five major oxides(Al_2O_3, CaO, MgO, FeO and TiO_2) are available in the repository Zenodo via DOIs: https://doi.org/10.5281/zenodo.7262473, https://doi.org/10.5281/zenodo. 7263324, https://doi.org/10.5281/zenodo.7263425, https://doi. org/10.5281/zenodo.7263592, https://doi.org/10.5281/zenodo. 7264328, and https://doi.org/10.5281/zenodo.7264372.

Declaration of Competing Interest

None.

Data availability

Data links are included in the acknowledgments.

Appendix A. Supplementary data

Supplementary data to this article can be found online at https://doi. org/10.1016/j.icarus.2023.115505.

References

Adams, J.B., Charette, M.P., 1975. Spectral reflectance of highland rock types at Apollo 17: evidence from Boulder 1, station 2. The Moon. 14 (3–4), 483–489. https://doi. org/10.1007/BF00569678.

Anguita, D., Ghio, A., Ridella, S., Sterpi, D., 2009. K-Fold Cross Validation for Error Rate Estimate in Support Vector Machines. International Conference on Data Mining. DBLP.

Anthony, M., Holden, S.B., 1998. Cross-validation for binary classification by real-valued functions: Theoretical analysis. Proc. of the. In: 11th Conf. On Computational Learning Theory, pp. 218–229.

Bhatt, M., et al., 2020. A comparison of elemental abundances derived from CHANDRAYAAN-2 class and CHANDRAYAAN-1 M³ from the Western nearside of the moon. In: Paper presented at 51rd Lunar and Planetary Science Conference (abstract # 2270).

Braden, S.E., Stopar, J.D., Robinson, M.S., et al., 2014. Evidence for basaltic volcanism on the moon within the past 100 million years. Nat. Geosci. 7 (11), 787–791. https://doi.org/10.1038/ngeo2252.

Charette, M.P., Mccord, T.B., Pieters, C.M., et al., 1974. Application of remote spectral reflectance measurements to lunar geology classification and determination of titanium content of lunar soils. J. Geophys. Res. 79, 1605–1613. https://doi.org/ 10.1029/JB079i011p01605.

Che, X., Nemchin, A., Liu, D., et al., 2021. Age and composition of young basalts on the moon, measured from samples returned by Chang'e-5. Science. 374 (6569), 887–890. https://doi.org/10.1126/science.abl7957.

Chen, Y., Jiang, H., Li, C., Jia, X., Ghamisi, P., 2016. Deep feature extraction and classification of hyperspectral images based on convolutional neural networks. IEEE Trans. Geosci. Remote Sens. 54, 6232–6251. https://doi.org/10.1109/ TGRS.2016.2584107.

Chen, X., He, X.Y., Zhou, G.X., Wang, B., Feng, G., Yu, H., Ji, Y., 2019. Fast and accurate decoding of Raman spectra-encoded suspension arrays using deep learning. Analyst. 144 (14), 4312–4319. https://doi.org/10.1039/C9AN00913B.

Crites, S.T., Lucey, P.G., 2015. Revised mineral and mg # maps of the moon from integrating results from the lunar prospector neutron and gamma-ray spectrometers with Clementine spectroscopy. Am. Mineral. 100 (4), 973–982. https://doi.org/ 10.2138/am-2015-4874.

Fu, X.H., Li, C.L., Zhang, G.L., et al., 2014. Data processing for the active particle-induced X-ray spectrometer and initial scientific results from Chang'e-3 mission. Res. Astron. Astrophys. 14, 1595–1606. https://doi.org/10.1088/1674-4527/14/12/008.

Giguere, T.A., Taylor, G.J., Hawke, B.R., et al., 2000. The titanium contents of lunar mare basalts. Meteorit. Planet. Sci. 35 (1), 193–200. https://doi.org/10.1111/j.1945-5100.2000.tb01985.x.

Gillis, J.J., Jolliff, B.L., Elphic, R.C., 2003. A revised algorithm for calculating TiO$_2$ from Clementine UVVIS data: a synthesis of rock, soil, and remotely sensed TiO$_2$ concentrations. J. Geophys. Res. 108 (E2) https://doi.org/10.1029/2001JE001515.

Gillis, J.J., Jolliff, B.L., Korotev, R.L., 2004. Lunar surface geochemistry: global concentrations of Th, K, and FeO as derived from lunar prospector and Clementine data. Geochem. Cosmochim. Acta. 68 (18), 3791–3805. https://doi.org/10.1016/j.gca.2004.03.024.

Glorot, X., Bordes, Y., Bengio, Y., 2011. Deep sparse rectifier neural networks. In: Proceedings of The Fourteenth International Conference on Artificial Intelligence and Statistics, JMLR Workshop and Conference Proceedings, pp. 315–323.

Glotch, T.D., Hagerty, J.J., Lucey, P.G., et al., 2011. The Mairan domes: silicic volcanic constructs on the moon. Geophys. Res. Lett. 38 (21) https://doi.org/10.1029/2011GL049548.

Haggerty, S.E., 1972. Luna 16: an opaque mineral study and a systematic examination of compositional variations of spinels from Mare Fecunditatis. Earth Planet. Sci. Lett. 13 (2), 328–352. https://doi.org/10.1016/0012-821X(72)90109-4.

Hapke, B., Cassidy, W., Wells, E., 1975. Effects of vapor-phase deposition processes on the optical, chemical, and magnetic properties OE the lunar regolith. The Moon. 13 (1–3), 339–353. https://doi.org/10.1007/BF00567525.

Head, J.W., Gifford, A., 1980. Lunar Mare domes: classification and modes of origin. The Moon and the Planets 22 (2), 235. https://doi.org/10.1007/BF00898434.

Heiken, G., Vaniman, D., French, B.M., 1991. Lunar Source Book. Cambridge University Press, New York, pp. 357–474.

Jia, B., Fa, W., Xie, M., Tai, Y., Liu, X., 2021. Regolith properties in the Chang'E-5 landing region of the moon: results from multi-source remote sensing observations. J. Geophys. Res., Planets. 126 https://doi.org/10.1029/2021JE006934 e2021JE006934.

Jia, B., Fa, W., Zhang, M., Di, K., Xie, M., Tai, Y., Li, Y., 2022. On the provenance of the Chang'E-5 lunar samples. Earth Planet. Sci. Lett. 596, 117791 https://doi.org/10.1016/j.epsl.2022.117791.

Jolliff, B.L., Gillis, J.J., Haskin, L.A., et al., 2000. Major lunar crustal terranes: surface expressions and crust-mantle origins. J. Geophys. Res.: Planets. 105 (E2), 4197–4216. https://doi.org/10.1029/1999JE001103.

Ketkar, N., 2017. Introduction to keras. In: Deep Learning with Python. Apress, Berkeley, CA, pp. 97–111.

Kingma, D.P., Ba, J., 2014. Adam: a method for stochastic optimization. arXiv preprint arXiv. https://doi.org/10.48550/arXiv.1412.6980, 1412.6980.

Laneuville, M., Breuer, D., Plesa, A.-C., Schwinger, S., 2017. Lunar surface Mg # distribution and Magma Ocean crystallization. In: Paper Presented at 48 rd Lunar and Planetary Science Conference (abs. #1434).

Lecun, Y., Bottou, Y., et al., 1998. Gradient-based learning applied to document recognition. Proc. IEEE 86 (11), 2278–2324.

Lemelin, M., Lucey, P.G., Song, E., Taylor, G.J., 2015. Lunar central peak mineralogy and iron content using the Kaguya multiband imager: reassessment of the compositional structure of the LUNAR crust: LUNAR CENTRAL PEAK MINERALOGY AND IRON. J. Geophys. Res.: Planets. 120 (5), 869–887. https://doi.org/10.1002/2014JE004778.

Lemelin, M., Lucey, P.G., Gaddis, L.R., Hare, T., Ohtake, M., 2016. Global map products from the Kaguya multiband imager at 512 ppd: minerals, FeO and OMAT. In: Paper Presented at 43 rd Lunar and Planetary Science Conference (abs. #2994).

Li, Q.L., et al., 2021. Two-billion-year-old volcanism on the moon from Chang'e-5 basalts. Nature. 600, 54–58. https://doi.org/10.1038/s41586-021-04100-2.

Li, C., Hu, H., Yang, M., Pei, Z., Zhou, Q., Ren, X., et al., 2022. Characteristics of the lunar samples returned by the Chang'E-5 mission. Natl. Sci. Rev. 9 (2) https://doi.org/10.1093/nsr/nwab188 nwab188.

Liebermann, R.C., Ringwood, A.E., 1976. Elastic properties of anorthite and the nature of the lunar crust. Earth Planet. Sci. Lett. 31 (1), 69–74. https://doi.org/10.1016/0012-821X(76)90097-2.

Ling, Z.C., Zhang, J., Liu, J.Z., et al., 2010. Preliminary results of FeO mapping from Chang'E-1 IIM data (in Chinese). Chin. Sci. Bull. 55 (35), 3373–3377.

Ling, Z.C., Zhang, J., Liu, J.Z., et al., 2011. Preliminary results of TiO$_2$ mapping using imaging interferometer data from Chang'E-1 (in Chinese). Chin. Sci. Bull. 56 (16), 1257–1263.

Ling, Z., Jolliff, B.L., Wang, A., Li, C., Liu, J., Zhang, J., et al., 2015. Correlated compositional and mineralogical investigations at the Chang'e-3 landing site. Nat. Commun. 6 (1), 1–9. https://doi.org/10.1038/ncomms9880.

Lu, Y., Wu, Y.Z., Li, C., et al., 2021. Seamless maps of major elements of the moon: results from high-resolution geostationary satellite. Res. Astron. Astrophys. 21 (2), 031. https://doi.org/10.1088/1674-4527/21/2/31.

Lucey, P.G., Taylor, G.J., Malaret, E., 1995. Abundance and distribution of iron on the moon. Science. 268 (5214), 1150–1153. https://doi.org/10.1126/science.268.5214.1150.

Lucey, P.G., Blewett, D.T., Hawke, B.R., 1998. Mapping the FeO and TiO$_2$ content of the lunar surface with multispectral imagery. J. Geophys. Res. 103 (E2), 3679. https://doi.org/10.1029/97JE03019.

Lucey, P.G., Blewett, D.T., Jolliff, B.L., 2000. Lunar iron and titanium abundance algorithms based on final processing of Clementine ultraviolet-visible images. J. Geophys. Res. 105 (E8), 20297. https://doi.org/10.1029/1999JE001117.

Lucey, P.G., Korotev, R.L., Gillis, J.J., Taylor, L.A., Lawrence, D.J., Campbell, B.A., Elphic, R.C., Feldman, B., Hood, L.L., Hunten, D.M., 2006. Understanding the lunar surface and space-moon interactions. Rev. Mineral. Geochem. 60 (1), 83–219. https://doi.org/10.2138/rmg.2006.60.2.

Ma, M., Li, B., Chen, S., et al., 2022. Global estimates of lunar surface chemistry derived from LRO diviner data. Icarus. 371 (4020), 114697 https://doi.org/10.1016/j.icarus.2021.114697.

Malek, S., Melgani, F., Bazi, Y., 2018. One- dimensional convolutional neural networks for spectroscopic signal regression. J. Chemom. 32 (e2977) https://doi.org/10.1002/cem.2977.

McCord, T.B., Charette, M.P., Johnson, T.V., Lebofsky, L.A., Pieters, C., Adams, J.B., 1972. Lunar spectral types. J. Geophys. Res. 77, 1349–1359.

Ohtake, M., Haruyama, J., et al., 2008. Performance and scientific objectives of the SELENE (KAGUYA) multiband imager. Earth Planet. & Space. 60 (4), 257–264. https://doi.org/10.1186/BF03352789.

Ohtake, M., Takeda, H., Matsunaga, T., Yokota, Y., Haruyama, J., Morota, T., Yamamoto, S., Ogawa, Y., Hiroi, T., Karouji, Y., 2012. Asymmetric crustal growth on the moon indicated by primitive farside highland materials. Nat. Geosci. 5 (6), 384–388. https://doi.org/10.1038/ngeo1458.

Ohtake, M., Pieters, C.M., Isaacson, P.J., Besse, S., Yokota, Y., Matsunaga, T., Boardman, J., Yamomoto, S., Haruyama, J., Staid, M., 2013. One moon, many measurements 3: spectral reflectance. Icarus. 226 (1), 364–374. https://doi.org/10.1016/j.icarus.2013.05.010.

Otake, H., Ohtake, M., Hirata, N., 2012. Lunar iron and titanium abundance algorithms based on SELENE (kaguya) multiband imager data. In: Paper Presented at 43 rd Lunar and Planetary Science Conference (abs. #1905).

Papike, J.J., 1988. Chemistry of the rock-forming silicates: multiple-chain, sheet, and framework structures. Rev. Geophys. 26 (3), 407–444. https://doi.org/10.1029/RG026i003p00407.

Pieters, C.M., Taylor, L.A., Noble, S.K., Keller, L.P., Hapke, B., Morris, R.V., et al., 2000. Space weathering on airless bodies: resolving a mystery with lunar samples. Meteorit. Planet. Sci. 35 (5), 1101–1107. https://doi.org/10.1111/j.1945-5100.2000.tb01496.x.

Prettyman, T.H., Hagerty, J.J., Elphic, R.C., et al., 2006. Elemental composition of the lunar surface: analysis of gamma ray spectroscopy data from lunar prospector. J. Geophys. Res.: Planets. 111 (E12) https://doi.org/10.1029/2005JE002656.

Qian, Y., Xiao, L., Head, J.W., van der Bogert, C.H., Hiesinger, H., Wilson, L., 2021a. Young lunar mare basalts in the Chang'e-5 sample return region, northern Oceanus Procellarum. Earth Planet. Sci. Lett. 555, 116702 https://doi.org/10.1016/j.epsl.2020.116702.

Qian, Y., Xiao, L., Wang, Q., Head, J.W., Yang, R., Kang, Y., vander Bogert, C.H., Hiesinger, H., Lai, X., Wang, G., Pang, Y., Zhang, N., Yuan, Y., He, Q., Huang, J., Zhao, J., Wang, J., Zhao, S., 2021b. China's Chang'e-5 landing site: geology, stratigraphy, and provenance of materials. Earth Planet. Sci. Lett. 561, 116855 https://doi.org/10.1016/j.epsl.2021.116855.

Qiao, L., Head, J.W., Xiao, L., Wilson, L., Dufek, J.D., 2018. The role of substrate characteristics in producing anomalously young crater retention ages in volcanic deposits on the moon: morphology, topography, subresolution roughness and mode of emplacement of the Sosigenes lunar irregular mare patch. Meteorit. Planet. Sci. 53 (4), 778. https://doi.org/10.1111/maps.13003.

Qiao, L., Head, J.W., Ling, Z., Wilson, L., 2020. Lunar irregular Mare patches: classification, characteristics, geologic settings, updated catalog, origin, and outstanding questions. J. Geophys. Res.: Planet. 125 (7) https://doi.org/10.1029/2019JE006362.

Qiu, D., Li, F., Yan, J., et al., 2021. Machine learning for inversing FeO and TiO$_2$ content on the moon: method and comparison. Icarus. 373 https://doi.org/10.1016/j.icarus.2021.114778.

Sato, H., Robinson, M.S., Lawrence, S.J., Denevi, B.W., Hapke, B., Jolliff, B.L., Hiesinger, H., 2017. Lunar mare TiO$_2$ abundances estimated from UV/Vis reflectance. Icarus. 296, 216–238. https://doi.org/10.1016/j.icarus.2017.06.013.

Stooke, P., 2012. Lunar meniscus hollows. In: Paper Presented at Lunar and Planetary Science Conference, (abs. #1011).

Sun, L., Ling, Z., Zhang, J., Li, B., Chen, J., Wu, Z., Liu, J., 2016. Lunar iron and optical maturity mapping: results from partial least squares modeling of Chang'E-1 IIM data. Icarus. 280, 183–198. https://doi.org/10.1016/j.icarus.2016.07.010.

Surkov, Y., Shkuratov, Y., Kaydash, V., Korokhin, V., Videen, G., 2020. Lunar ilmenite content as assessed by improved Chandrayaan-1 M3 data. Icarus. 341, 113661 https://doi.org/10.1016/j.icarus.2020.113661.

Taylor, S.R., 1987. The unique lunar composition and its bearing on the origin of the moon. Geochim. Cosmochim. Acta 51 (5), 1297–1309. https://doi.org/10.1016/0016-7037(87)90220-1.

Taylor, G.J., Warren, P., Ryder, G., et al., 1991. Lunar Sourcebook. Cambridge University Press, Cambridge, pp. 183–284.

Tian, H.C., Wang, H., Chen, Y., et al., 2021. Non-KREEP origin for Chang'e-5 basalts in the Procellarum KREEP terrane. Nature. 600, 7887. https://doi.org/10.1038/s41586-021-04119-5.

Wang, X., Zhang, J., Ren, H., 2021. Lunar surface chemistry observed by the KAGUYA multiband imager. Planet. Space Sci. 209, 105360 https://doi.org/10.1016/j.pss.2021.105360.

Wilcox, B.B., Lucey, P.G., Gillis, J.J., 2005. Mapping iron in the lunar mare: an improved approach. J. Geophys. Res. 110 (E11) https://doi.org/10.1029/2005JE00251.

Wu, Y., 2012. Major elements and mg# of the moon: results from Chang'E-1 interference imaging spectrometer (IIM) data. Geochim. Cosmochim. Acta 93, 214–234. https://doi.org/10.1016/j.gca.2012.07.011.

Xia, W., Wang, X., Zhao, S., Jin, H., Chen, X., Yang, M., et al., 2019. New maps of lunar surface chemistry. Icarus. 321, 200–215. https://doi.org/10.1016/j.icarus.2018.10.031.

Yan, B., Xiong, S.Q., Wu, Y., et al., 2012. Mapping lunar global chemical composition from Chang'E-1 IIM data. Planet. Space Sci. 67 (1), 119–129. https://doi.org/10.1016/j.pss.2012.03.010.

Yuan, Q., Wang, J., Zheng, M., et al., 2022. Hybrid 1D-CNN and attention-based bi-GRU neural networks for predicting moisture content of sand gravel using NIR

spectroscopy. Constr. Build. Mater. 350, 128799 https://doi.org/10.1016/j.conbuildmat.2022.128799.

Zhang, J., Yang, W., Hu, S., et al., 2015. Volcanic history of the imbrium basin: a close-up view from the lunar rover yutu. Proc. Natl. Acad. Sci. U. S. A. 112 (17), 5342–5347.

Zong, K., et al., 2022. Bulk compositions of the Chang'E-5 lunar soil: insights into chemical homogeneity, exotic addition, and origin of landing site basalts. Geochim. Cosmochim. Acta 335, 284–296. https://doi.org/10.1016/j.gca.2022.06.037.